Cite this: *Dalton Trans.*, 2021, **50**, 926

Synthesis, characterization, and electrocatalytic activity of bis(pyridylimino)isoindoline Cu(II) and Ni(II) complexes†

Soumen Saha,^a Sha Tamanna Sahil,^b Md. Motiur R. Mazumder,^a Alexander M. Stephens,^a Bryan Cronin,^a Evert C. Duin,^a Jonah W. Jurs ^b and Byron H. Farnum ^{*a}

Two NNN pincer complexes of Cu(II) and Ni(II) with BPI_{Me}[−] [BPI_{Me}[−] = 1,3-bis((6-methylpyridin-2-yl)imino)isoindolin-2-ide] have been prepared and characterized structurally, spectroscopically, and electrochemically. The single crystal structures of the two complexes confirmed their distorted trigonal bipyramidal geometry attained by three equatorial N-atoms from the ligand and two axially positioned water molecules to give [Cu(BPI_{Me})(H₂O)₂]ClO₄ and [Ni(BPI_{Me})(H₂O)₂]ClO₄. Electrochemical studies of Cu(II) and Ni(II) complexes have been performed in acetonitrile to identify metal-based and ligand-based redox activity. When subjected to a saturated CO₂ atmosphere, both complexes displayed catalytic activity for the reduction of CO₂ with the Cu(II) complex displaying higher activity than the Ni(II) analogue. However, both complexes were shown to decompose into catalytically active heterogeneous materials on the electrode surface over extended reductive electrolysis periods. Surface analysis of these materials using energy dispersive spectroscopy as well as their physical appearance suggests the reductive deposition of copper and nickel metal on the electrode surface. Electrocatalysis and decomposition are proposed to be triggered by ligand reduction, where complex stability is believed to be tied to fluxional ligand coordination in the reduced state.

Received 30th August 2020,
Accepted 7th December 2020

DOI: 10.1039/d0dt03030a

rsc.li/dalton

Introduction

Meridionally coordinating tridentate ligands, so-called ‘pincer’ ligands, have been extensively studied in inorganic, organometallic, and molecular catalysis.^{1–5} Among this class of ligands (*e.g.* NCN,^{6–8} CNC,^{9–11} NNN,^{12–15} and PNP,^{16–19} where letters represent the atomic nature of each coordinating atom), bis(pyridylimino) isoindoles (BPIH, NNN) are of interest because of their ease of synthesis, thermal stability, and tunability by modification of the aromatic rings. A broad range of derivatized BPIH ligands have been reported as metal chelators and their coordination chemistry has been explored since the late twentieth century.^{20–22} These ligands act as anionic chelating pincer ligands (*i.e.* BPI[−]) in the presence of weak

base and may coordinate to the metal center to form either 2 : 1 (ligand : metal) or 1 : 1 complexes.²²

In recent years utilization of these transition metal BPI[−] complexes toward energy storage and catalysis have become active research areas.^{23–30} For example, several first-row metal BPI[−] complexes have been shown to act as potential anolyte materials for nonaqueous redox flow batteries.²³ These pseudo octahedral 2 : 1 complexes displayed multiple, reversible ligand-based redox potentials. The reversibility of the redox events and the stability of the complexes over multiple charge-discharge cycles was attributed to the strong chelating environment and coordination saturation of the metal center. In terms of catalysis, 1 : 1 complexation between BPI[−] and the metal is preferred to have open coordination sites at the metal center.^{25,30–32} As an example, a series of κ²-(N,N) and κ³-(N,N,N) coordinated iridium and osmium complexes were reported to be catalytically active in the transfer hydrogenation of ketones and imines.³¹ A variety of BPI[−] derivatives have been shown to produce 1 : 1 complexes, however, one strategy which encourages their formation is to install sterically bulky substituents in the *ortho* position relative to the pyridine nitrogen. Derivatization at this position discourages coordination in the equatorial plane and promotes axial coordination above and

^aDepartment of Chemistry and Biochemistry, Auburn University, Auburn, AL 36832, USA. E-mail: farnum@auburn.edu

^bDepartment of Chemistry and Biochemistry, University of Mississippi, University, MS 38677, USA

† Electronic supplementary information (ESI) available: X-ray crystal structures, crystallographic data, CV, SEM/EDS, ESI-MS, ATR-IR and NMR. CCDC 2006230, 2012499, 1904565 and 1913288. For ESI and crystallographic data in CIF or other electronic format see DOI: 10.1039/d0dt03030a

below the BPI⁻ ligand. This strategy has been used in particular toward asymmetric catalysis using chiral BPI⁻ ligands.¹³

In this context we report the synthesis and catalytic properties of Cu(II) and Ni(II) complexes containing a BPI⁻ ligand derivatized with a methyl group at the *ortho* position relative to each pyridine nitrogen, BPI_{Me}H. This functionalization is shown to discourage the formation of 2:1 complexes and forms the corresponding [Cu(BPI_{Me})(H₂O)₂]₂ClO₄ ([Cu-BPI_{Me}]⁺) and [Ni(BPI_{Me})(H₂O)₂]₂ClO₄ ([Ni-BPI_{Me}]⁺) species. To our knowledge, these complexes have not been previously reported in the literature. Characterization of their physical properties was performed using single crystal X-ray diffraction, UV-visible absorption spectroscopy, electron paramagnetic spectroscopy, and electrochemistry. The electrocatalytic reduction of CO₂ by each complex was also assessed, where [Cu-BPI_{Me}]⁺ exhibited more electrocatalytic behavior compared to [Ni-BPI_{Me}]⁺ with each producing CO as product. Both complexes, however, were found to decompose to heterogeneous materials over extended electrolysis periods. These decomposition products were also found to be catalytically active for CO₂ reduction to CO.

Experimental section

General considerations

All chemicals were used as received with the exception of *n*-tetrabutylammonium hexafluorophosphate (TBAPF₆), which was recrystallized twice prior to electrochemical experiments. ¹H and ¹³C NMR were recorded on a Bruker 600 MHz spectrometer using methanol-*d*₄ (Cambridge Isotope Laboratories, 99.8%). Chemical shifts are reported in parts per million (δ) and referenced against residual internal solvent signals. Mass spectrometry analyses were performed on a quadrupole time-of-flight mass spectrometer (Q-ToF Premier, Waters) with electrospray ionization (ESI) in positive mode using Masslynx software (V4.1). The samples were infused in acetonitrile *via* a syringe pump. Elemental analysis was performed by Atlantic Microlab with microcrystalline powder samples. UV-visible absorbance spectra were recorded on an Agilent HP 8454 diode array spectrophotometer in acetonitrile (MeCN) for all samples. Attenuated total reflectance Fourier transform infrared spectroscopy (ATR-IR) was performed using a Nicolet iS-50 spectrometer with a built-in diamond ATR. Characterization data for NMR, ATR-IR, and ESI-MS are given in the ESI.†

Electron paramagnetic resonance spectroscopy was performed using an X-band Bruker EMX spectrometer fitted with an ER-4119-HS (high-sensitivity) perpendicular-mode cavity. Samples were prepared by dissolving crystalline solid in MeCN and transferring to an EPR tube where the sample was frozen using liquid nitrogen. The spectra were recorded at 77 K with a field modulation frequency of 100 kHz, a modulation amplitude of 6.00 G, a microwave power of 1.995 mW, and a frequency of 9.366 GHz. EPR data were simulated using the program Hyperfine Spectrum (W R Hagen Visual Software, V 1.0, 2009).³³

Single crystal X-ray diffraction was carried out on a Bruker D8 VENTURE κ-geometry diffractometer using Cu Kα radiation

(Incoatec IμS DIAMOND microfocus sealed tube, λ = 1.54178 Å). The integrations and global cell refinements were performed by using APEX3 software which includes Bruker SAINT software package. Finally, the structures were solved by using Intrinsic Phasing/Direct Methods (ShelXT)^{34,35} and least-squares refinement was performed using ShelXL in APEX3. Olex 2 solvent mask was employed for [Cu₂(BPI_{Me})₂(OH)]ClO₄. Mask void volume: 187 Å³ volume corresponding to 68 electrons, closely matching three methanols and one water per unit cell.

Scanning electron microscopy (SEM) was performed using a Zeiss EVO 50VP scanning electron microscope with energy dispersive spectroscopy (EDS, INCA). SEM/EDS was performed on GC working electrodes following controlled potential electrolysis of each metal complex and a gentle rinse. Elemental peaks were calibrated using INCA software and a copper standard.

Caution! Metal complexes containing perchlorate ions are potentially explosive and should be used carefully.

Synthesis of 1,3-bis((6-methylpyridin-2-yl)imino)isoindolin (BPI_{Me}H)

The ligand BPI_{Me}H was synthesized by following a previously reported procedure with slight modifications to the extraction step.^{15,36,37} Phthalonitrile (Alfa Aesar, 98%, 2.56 g, 20.0 mmol) was added to a 3-necked round bottom flask along with CaCl₂ (Sigma Aldrich, ≥ 93%, 1.10 g, 9.20 mmol) and 2-methyl-6-aminopyridine (Sigma Aldrich 98%, 4.54 g, 42.0 mmol). The mixture was purged for 20 min with N₂ followed by addition of butanol (Sigma Aldrich, 99.8%, 30 mL) and an additional purge of 1 h with N₂. The reaction mixture was then refluxed for 48 h at 117 °C. Once the mixture cooled, a yellow-green precipitate was formed that was washed with water and filtered three times. After filtration, the green solid mixture was dissolved in dichloromethane (DCM, VWR, 99.5%) and subjected to extraction with water (1:1, 3 times) to remove any excess salt. The organic layer was evaporated to dryness and the final product was recrystallized in methanol (MeOH, VWR, 98%) to result in a yellow microcrystalline powder. X-ray quality crystals were grown by dissolving the solid in DCM followed by slow evaporation at room temperature. Yield: 4.40 g, 67%. ATR-IR (cm⁻¹): 3277, 1633, 1556, 1438, 1203, 1146, 774, 677. UV-Vis (MeCN): 275 nm (ε/M⁻¹ cm⁻¹, 13 900), 367 nm (ε/M⁻¹ cm⁻¹, 12 400). ¹H-NMR: 7.99–7.97 (q, *J* = 6, 2H), 7.67–7.64 (m, *J* = 12, 4H), 7.09–7.07 (d, *J* = 12, 2H), 7.00–6.98 (d, *J* = 12, 2H), 2.35 (s, 6H) ppm. ¹³C-NMR: 161.08, 158.71, 154.79, 140.55, 136.41, 133.66, 123.90, 121.48, 119.18, 24.69 ppm. ESI mass (*m/z*) for [C₂₀H₁₇N₅ + H]⁺: calcd: 328.1562, found: 328.1555. Elemental analysis (%) for C₂₀H₁₇N₅: calcd: C, 73.37; H, 5.23; N, 21.39; found: C, 73.08; H, 5.38; N, 21.25.

Synthesis of [Cu(BPI_{Me})(H₂O)₂]₂ClO₄

BPI_{Me}H (0.327 g, 1.00 mmol) was added to 30 mL of MeOH with methanolic tetra-*n*-butylammonium hydroxide (TBAOH, Alfa Aesar, 1.0 mL, 1.0 M) and warmed at 50 °C for 1 h. A solution of Cu(ClO₄)₂·6H₂O (Sigma Aldrich, 98% 0.370 g, 0.966 mmol) in 10 mL MeOH was warmed at 50 °C and then

added to the stirring mixture. After 1 h, the solution was filtered to remove unreacted solid. The filtrate was collected and evaporated to dryness. The resulting solid was washed with 50 mL DCM and dried in air. X-ray quality crystals were grown by dissolving the solid in MeOH followed by slow evaporation at room temperature. Yield 0.40 g, 79%. ATR-IR (cm^{-1}): 3402, 1583, 1518, 1446, 1192, 1041, 782, 708, 619, 511. UV-Vis (MeCN) 277 nm ($\epsilon/\text{M}^{-1} \text{cm}^{-1}$, 22 500), 322 nm ($\epsilon/\text{M}^{-1} \text{cm}^{-1}$, 25 800), 338 nm ($\epsilon/\text{M}^{-1} \text{cm}^{-1}$, 23 100), 431 nm ($\epsilon/\text{M}^{-1} \text{cm}^{-1}$, 25 300), 459 nm ($\epsilon/\text{M}^{-1} \text{cm}^{-1}$, 21 400) ESI mass (m/z) for $[\text{C}_{20}\text{H}_{16}\text{N}_5\text{Cu}]^+$: calcd: 389.0701, found: 389.0733. Elemental analysis (%) for $\text{C}_{20}\text{H}_{20}\text{N}_5\text{CuClO}_6$: calcd: C, 45.72; H, 3.84; N, 13.33; found: C, 45.59; H, 3.87; N, 13.23.

Synthesis of $[\text{Cu}_2(\text{BPI}_{\text{Me}})_2(\text{OH})]\text{ClO}_4$

$\text{BPI}_{\text{Me}}\text{H}$ ligand (0.654 g, 2.00 mmol) along with triethylamine (TEA, Sigma Aldrich, >99%, 418 μL , 3.00 mmol) was added to a 30 mL 1 : 1 mixture of MeCN (VWR, 99.95%)/DCM. A solution of $\text{Cu}(\text{ClO}_4)_2 \cdot 6\text{H}_2\text{O}$ (0.740 g, 1.93 mmol) in 10 mL of MeCN was then added to the stirring ligand solution. After 1 h, the solution was filtered, the green solid was collected, washed with 50 mL of dichloromethane, and recrystallized in MeOH. X-ray quality crystals were obtained by vapor diffusion of diethyl ether over MeOH solution at room temperature. Yield 0.60 g, 62%. ATR-IR (cm^{-1}): 3402, 1583, 1523, 1438, 1188, 1086, 804, 706, 617, 513. UV-Vis (MeCN): 277 nm ($\epsilon/\text{M}^{-1} \text{cm}^{-1}$, 22 800), 316 nm ($\epsilon/\text{M}^{-1} \text{cm}^{-1}$, 26 400), 340 ($\epsilon/\text{M}^{-1} \text{cm}^{-1}$, 24 400), 430 nm ($\epsilon/\text{M}^{-1} \text{cm}^{-1}$, 21 800), 460 nm ($\epsilon/\text{M}^{-1} \text{cm}^{-1}$, 16 000) ESI mass (m/z) for $[\text{C}_{40}\text{H}_{33}\text{N}_5\text{OCu}_2]^+$: calcd: 795.1523. Found: 389.0708 (50%), 390.0777 (100%). The observed masses indicate the dissociation of the complex into two units of $[\text{Cu}(\text{BPI}_{\text{Me}})]^+$. The mass of 389.0708 is consistent with $[\text{Cu}^{\text{II}}(\text{BPI}_{\text{Me}})]^+$ while the mass of 390.0777 is consistent with $[\text{Cu}^{\text{I}}(\text{BPI}_{\text{Me}}\text{H})]^+$. We believe the reduction of the copper center and protonation occur during the ESI-MS experiment as such events have been previously observed in the literature.^{38,39} ESI⁺ shows simulations of calculated spectra based on a mixture of ions. Elemental Analysis for $\text{C}_{40}\text{H}_{33}\text{N}_5\text{Cu}_2\text{ClO}_5$: calcd: C, 53.60; H, 3.71; N, 15.63 (%); found: C, 53.17; H, 3.50; N, 15.53 (%).

Synthesis of $[\text{Ni}(\text{BPI}_{\text{Me}})(\text{H}_2\text{O})_2]\text{ClO}_4$

$\text{BPI}_{\text{Me}}\text{H}$ ligand (0.327 g, 1.00 mmol) along with triethylamine (TEA, Sigma Aldrich, $\geq 99\%$, 209 μL , 1.50 mmol) was added to a 30 mL MeCN/DCM (1 : 1) mixture. A solution of $\text{Ni}(\text{ClO}_4)_2 \cdot 6\text{H}_2\text{O}$ (STREM, 99%, 0.365 g, 0.975 mmol) in 10 mL of MeCN was then added to the stirring ligand mixture. After 1 h, the solution was filtered and the green solid was further washed by 50 mL of DCM and recrystallized in MeOH. X-ray quality crystals were obtained by vapor diffusion of diethyl ether over a methanol solution at room temperature. Yield 0.41 g, 81%. ATR-IR (cm^{-1}): 3384, 1579, 1509, 1448, 1189, 1034, 899, 778, 710, 620, 518. UV-Vis (MeCN): 289 nm ($\epsilon/\text{M}^{-1} \text{cm}^{-1}$, 15 300), 321 nm ($\epsilon/\text{M}^{-1} \text{cm}^{-1}$, 23 800), 337 nm ($\epsilon/\text{M}^{-1} \text{cm}^{-1}$, 20 600), 431 nm ($\epsilon/\text{M}^{-1} \text{cm}^{-1}$, 30 000), 460 nm ($\epsilon/\text{M}^{-1} \text{cm}^{-1}$, 28 800). ESI mass (m/z) for $[\text{C}_{20}\text{H}_{16}\text{N}_5\text{Ni}]^+$: calcd: 384.0759, found: 384.0841. Elemental analysis (%) for

$\text{C}_{20}\text{H}_{20}\text{N}_5\text{NiClO}_6$: calcd: C, 46.15; H, 3.87; N, 13.45; found: C, 45.96; H, 3.94; N, 13.42.

Electrochemistry

TBAPF₆ (Sigma Aldrich, 98%) was recrystallized twice in absolute ethanol (KOPTEC, 200 proof), washed with diethyl ether (Avantor, 99%), dried under vacuum, and stored in a desiccator. All cyclic voltammetry (CV) experiments were performed in MeCN with 0.1 M TBAPF₆ electrolyte purged with either N₂ or CO₂ (Bone dry, Airgas). Experiments were performed at room temperature using a CH Instruments 600E Series potentiostat with a glassy carbon (GC) disk working electrode (3 mm diameter, BASi), a Ag/Ag⁺ nonaqueous reference electrode (BASi) with 0.001 M AgNO₃ (BASi) in MeCN, and a platinum wire counter electrode (BASi). The GC working electrode was polished with 0.05 μm alumina powder (Allied High Tech Products Inc., DeAgglomerated). The reduction potential of ferrocene (Fc; Alfa Aesar, 99%) was recorded before and after all electrochemical experiments in a separate MeCN (0.1 M TBAPF₆) solution to confirm the consistency of the reference electrode. All potentials are reported *versus* the Fc⁺⁰ couple. All data were collected after compensating for the internal solution resistance and consisted of three continuous cycles scanned with an initial negative direction over the potential range. Data shown are those of the third cycle.

Controlled potential electrolysis (CPE) experiments were performed in a 3-neck pear-shaped glass cell with a GC rod (2 mm diameter, type 2, Alfa Aesar) working electrode, a silver wire quasi-reference electrode, and a platinum mesh (2.5 cm² area, 150 mesh) counter electrode that was housed in an isolation chamber, separated from the other electrodes with a fine glass frit. Solutions were degassed with CO₂ for 30 min before collecting data. Applied potentials in CPE experiments were determined by cyclic voltammetry. Constant stirring was maintained during electrolysis. Headspace gases in the airtight vessel were analyzed by gas chromatography using a custom PerkinElmer Clarus 680 Gas Chromatograph (Agilent PorapakQ column, 6 ft, 1/8 in. OD) with a dual detector system (TCD and FID). Integrated gas peaks were quantified with calibration curves generated from known standards purchased from BuyCalGas.com. CO was measured at an FID detector equipped with a methanizer, while H₂ was quantified at the TCD detector. Faradaic efficiencies were determined from the experimental amount of product formed during electrolysis divided by the theoretical amount of product possible based on accumulated charge passed and the electron stoichiometry of the reaction $\times 100$.

CPE experiments on GC disk electrodes used for SEM/EDS analysis were performed with a Pine Wavedriver 20 Bipotentiostat. A rotating disk electrode (RDE) with interchangeable GC disks (5 mm diameter, Pine Research) was used as the working electrode with a Ag/Ag⁺ nonaqueous reference electrode (BASi) with 0.001 M AgNO₃ (BASi) in MeCN, and a platinum mesh counter electrode. All experiments were performed on freshly polished GC disk electrodes in CO₂-saturated MeCN with 0.1 M TBAPF₆ electrolyte at the indicated

applied potentials under constant stirring. Following CPE experiments, GC disk electrodes were removed from the RDE and gently rinsed with acetone before analysis with SEM/EDS.

Results and discussion

The ligand BPI_{Me}H (Fig. 1) containing methyl groups in the *ortho* position with respect to the pyridine nitrogen was synthesized by following an earlier literature procedure.^{15,36,37} Single crystal X-ray crystallography revealed that BPI_{Me}H crystallizes with a dimeric asymmetric unit with one pyridine ring puckered above the isoindole-pyridine plane (Fig. S3†) This is believed to be the result of π - π interactions between neighboring molecules and the steric repulsion of *ortho*-methyl groups. The crystallographic parameters are closely matched with an earlier report of this ligand structure.⁴⁰

Coordination of Cu(II) and Ni(II) were achieved with a mixture of 1 eq. of BPI_{Me}H and 1 eq. Cu(ClO₄)₂·6H₂O or Ni(ClO₄)₂·6H₂O in MeOH at room temperature in the presence of base. In the case of Cu(II), the base used for deprotonation of BPI_{Me}H resulted in either a mononuclear (TBAOH) or dinuclear (TEA) Cu(II) 1 : 1 ligand : metal complex. Similar dinuclear coordination between BPI⁻ ligands and Cu(II) has also been observed in the literature.^{41,42} In the case of Ni(II), the 1 : 1 mononuclear complex was produced with both TBAOH and TEA.

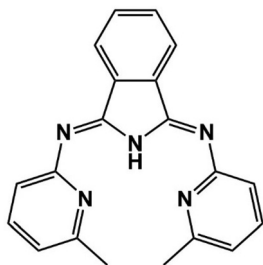


Fig. 1 Chemical structure of BPI_{Me}H ligand.

Solid state crystal structures of the mononuclear complexes [Cu(BPI_{Me})(H₂O)₂]ClO₄ ([Cu-BPI_{Me}]⁺) and [Ni(BPI_{Me})(H₂O)₂]ClO₄ ([Ni-BPI_{Me}]⁺) are shown in Fig. 2. Their structures are highly similar, with coordination by three N-atoms from the ligand and two water molecules positioned axially to attain a distorted trigonal bipyramidal geometry. The average Cu-N_{py} (2.028 Å) and Ni-N_{py} (2.077 Å) distances were found within the range of similar reported complexes.^{41–43} The shorter distances for Cu-N_{ind} (1.937 Å), Ni-N_{ind} (1.933 Å), and the backbone C=N (1.297 Å/1.303 Å; Cu/Ni) distances suggests the coordination of anionic BPI_{Me}⁻ to the respective metal centers. In the free BPI_{Me}H ligand, one of the pyridine rings is twisted from the plane (torsion angle; C7-N2-C6-N1 ~31.34°) because of the presence of the *ortho* methyl groups in the π - π stacking dimeric unit. Upon complexation to both Cu(II) and Ni(II), the two pyridine rings become coplanar with torsion angles of 6.5° for [Cu-BPI_{Me}]⁺ and 1.1° for [Ni-BPI_{Me}]⁺. Additionally, the position of the metal center in the coordination pocket is almost perfectly T-shaped with average angles for N_{py}-Cu-N_{ind} of 91.78° and N_{py}-Ni-N_{ind} of 91.24°. The bond angles for N_{py}-Cu-N_{py} (176.43°) and N_{py}-Ni-N_{py} (176.81°) are nearly linear. However, the two axially positioned water molecules differ between the two complexes by 14°; O-Cu-O (141.23°) and O-Ni-O (155.23°). Interestingly, the presence of the *o*-methyl groups in [Cu-BPI_{Me}]⁺ decreases the N_{ind}-Cu-O (108.06° and 110.68°) bond angle compared to an analogous Cu(II) complex (N_{ind}-Cu-O: 120.61° and 136.19°) having *p*-methyl substituents. This comparison highlights the steric repulsion of the *o*-methyl groups, resulting in coordinated water molecules which are distorted from the trigonal bipyramidal geometry to angles greater than 120°. Further crystallographic parameters are listed in the ESI.†

In contrast to the mononuclear complexes, the dinuclear [Cu₂(BPI_{Me})₂(OH)]ClO₄ complex (Fig. S4†) produced Cu(II) centers with distorted tetrahedral geometries with coordination from three N-atoms of the ligand and one μ -OH group bridged between the Cu(II) centers. The average Cu-O bond distance (1.928 Å) is similar with another reported μ -OH bridged Cu(II) complex.⁴¹

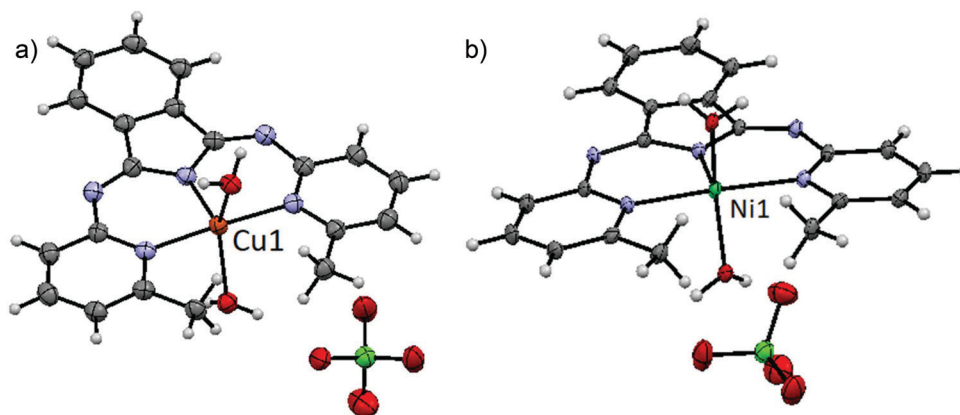


Fig. 2 ORTEP diagrams of (a) [Cu(BPI_{Me})(H₂O)₂]ClO₄ and (b) [Ni(BPI_{Me})(H₂O)₂]ClO₄ with thermal ellipsoids shown at 50% probability. Solvent molecules outside the coordination sphere are omitted for clarity.

In all structures reported here, the BPI_{Me}^- ligand design is shown to produce 1:1 ligand:metal complexes. We believe the *o*-methyl groups discourage the coordination of a fourth ligand in the equatorial plane around Cu(II) and Ni(II). However, we note that axial coordination is not predicated on *ortho* substitution, as Cu(II) and Ni(II) complexes with both axial and equatorial coordination have been reported with unsubstituted pyridine arms.^{44–46}

Fig. 3 shows the UV-visible extinction coefficient spectra of $[\text{Cu-BPI}_{\text{Me}}]^+$ and $[\text{Ni-BPI}_{\text{Me}}]^+$ in MeCN solution. Both complexes display similar spectra with a broad range of features between 200–475 nm and are overall similar to those observed for other transition metal and main group BPI^- complexes.⁴⁷ These absorption features have been assigned to $\pi-\pi^*$ transitions within the conjugated BPI_{Me}^- ligand, as the vibronic progression of peaks can be clearly observed. The frequency differences of these vibrational sublevels are nearly constant and close to 1440 cm^{-1} (Table S9[†]), which is consistent with a C–H bending mode and similar to what is observed in the electronic absorbance spectrum of anthracene.⁴⁸ Notably, these transitions are red shifted with respect to those of the free ligand. This observation has been previously assigned to an increase in planarity of the ligand structure, resulting in both the increase in molar absorptivity and red shift in energy.^{47,49,50} In some cases, such as Pt(II)-BPI complexes, mixed ligand-to-metal charge transfer character has been observed in the range of 450–600 nm.^{49,50} Given the similarity of the spectra for $[\text{Cu-BPI}_{\text{Me}}]^+$ and $[\text{Ni-BPI}_{\text{Me}}]^+$, we believe these transitions to be mostly $\pi-\pi^*$ in nature. As an added note, dissolution of $[\text{Cu}_2(\text{BPI}_{\text{Me}})_2(\text{OH})]\text{ClO}_4$ in MeCN resulted in an identical UV-visible absorbance spectrum as for $[\text{Cu-BPI}_{\text{Me}}]^+$. This would indicate dissociation of the dimer in solution to produce two equivalents of $[\text{Cu-BPI}_{\text{Me}}]^+$ and OH^- . Given the $\pi-\pi^*$ character of the absorbance spectrum, it is difficult to ascertain coordination of OH^- , H_2O , or MeCN to the metal center in solution. Mass spectrometry data indicated the

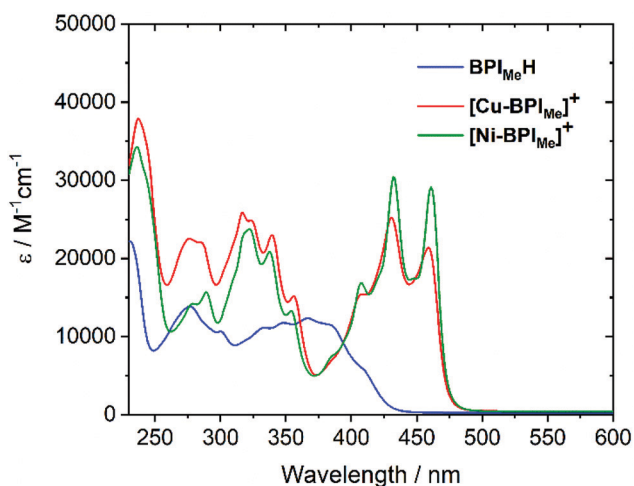


Fig. 3 UV-visible extinction coefficient spectra of $\text{BPI}_{\text{Me}}\text{H}$, $[\text{Cu-BPI}_{\text{Me}}]^+$, and $[\text{Ni-BPI}_{\text{Me}}]^+$ in MeCN.

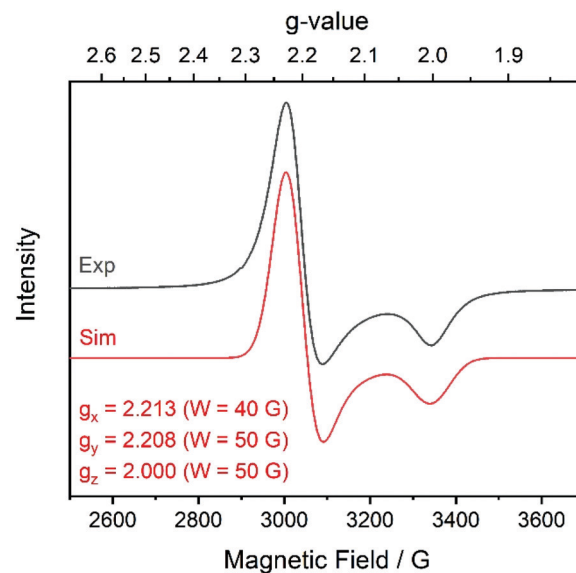


Fig. 4 EPR spectrum of 1 mM $[\text{Cu-BPI}_{\text{Me}}]^+$ in MeCN at 77 K. Parameters used for simulation: $g_x = 2.213$ ($W = 40\text{ G}$), $g_y = 2.208$ ($W = 50\text{ G}$), $g_z = 2.000$ ($W = 50\text{ G}$).

absence of any axial ligands; however, this could be an artifact of the desolvation process in the ESI-MS experiment (Fig. S7[†]).

Fig. 4 shows the X-band EPR spectrum of $[\text{Cu-BPI}_{\text{Me}}]^+$ collected at 77 K in MeCN. The signal was best simulated with $g_x = 2.213$ ($W = 40\text{ G}$), $g_y = 2.208$ ($W = 50\text{ G}$), and $g_z = 2.000$ ($W = 50\text{ G}$). The similarity of g_x and g_y ($g_{\perp,\text{avg}} = 2.211$) as well as g_z ($g_{\parallel} \sim g_e (=2.0023)$) gives a clear indication of a trigonal bipyramidal geometry around the $S = \frac{1}{2}$ d^9 metal center, consistent with the X-ray crystal structure. The difference between square planar and trigonal bipyramidal geometries in copper complexes has been correlated to the g_{\perp} and g_{\parallel} values, where $g_{\perp} > g_{\parallel}$ indicates trigonal bipyramidal and $g_{\perp} < g_{\parallel}$ indicates square planar.^{51–53} It is unclear whether the water molecules found in the X-ray crystal structure are responsible for axial coordination or if they have been replaced by MeCN. The linewidths for each g -tensor are notably broad (>40 Gauss) and could indicate unresolved hyperfine coupling to the $I = 3/2$ spin of the copper metal center. $[\text{Ni-BPI}_{\text{Me}}]^+$ was found to be EPR silent in the X-band region, consistent with an $S = 1$ spin-state and supported by $^1\text{H-NMR}$ which exhibited broad, paramagnetically shifted peaks.

Electrochemistry

Cyclic voltammograms of $[\text{Cu-BPI}_{\text{Me}}]^+$ and $[\text{Ni-BPI}_{\text{Me}}]^+$ in MeCN with 0.1 M TBAPF₆ electrolyte under an atmosphere of N₂ are shown in Fig. 5. Table 1 shows a summary of cathodic and anodic peak potentials (E_{pc} and E_{pa}) as well as $E_{1/2}$ ($(E_{\text{pa}} + E_{\text{pc}})/2$) potentials for $\text{BPI}_{\text{Me}}\text{H}$ and the series of complexes. For $[\text{Cu-BPI}_{\text{Me}}]^+$, three quasi-reversible redox waves with $E_{\text{pc}1} = -0.49\text{ V}$, $E_{\text{pc}2} = -1.82\text{ V}$, and $E_{\text{pc}3} = -2.32\text{ V}$ vs. $\text{Fc}^{+/0}$ were observed. $E_{\text{pc}1}$ is assigned to the Cu(II/I) redox couple while $E_{\text{pc}2}$ and $E_{\text{pc}3}$ are attributed to ligand-based reductions as both peaks are comparable to those observed for the free ligand

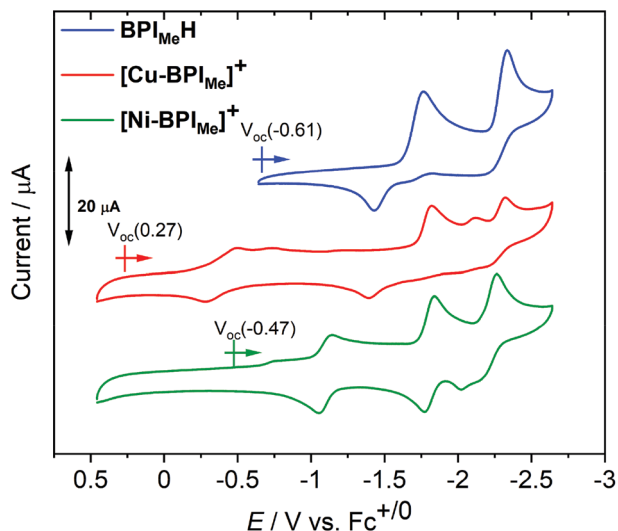


Fig. 5 CV data of 1 mM BPI_{Me}H (blue), 0.5 mM [Cu-BPI_{Me}]⁺ (red), and 0.5 mM [Ni-BPI_{Me}]⁺ (green) in MeCN under N₂ atmosphere with 0.1 M TBAPF₆. Scan rate: 100 mV s⁻¹. Arrows indicate the resting potential (V_{OC}) and initial scan direction.

BPI_{Me}H. DFT calculations for the LUMO of the BPI class of ligands indicate the electron for the first ligand-based reduction is within a π* orbital delocalized over the entire ligand structure.⁵⁰ We speculate that the reduction at E_{pc} = -2.20 V could be related to the Cu(I/0) redox couple. For [Ni-BPI_{Me}]⁺, similar ligand reductions at E_{pc2} = -1.84 V and E_{pc3} = -2.26 V were observed while the Ni(II/I) redox couple was shifted cathodically to E_{pc1} = -1.14 V with respect to the M(II/I) observed for [Cu-BPI_{Me}]⁺.

The reversibility of the first ligand-based reduction is notably higher for [Ni-BPI_{Me}]⁺ than for [Cu-BPI_{Me}]⁺ and BPI_{Me}H, with peak splitting (ΔE_p) values of 0.07, 0.43, and 0.33 V, respectively. We hypothesize that the reversibility, or lack thereof, for this wave is related to rotation of one of the pyridine arms out of the coordination pocket. Such fluxional behavior in this ligand class has been noted in the literature with examples of monometallic and bimetallic complexes showing coordination to the rotated N_{pyridine} in addition to a backbone N_{imine}.^{24,31} Trimetallic complexes have even been observed in the case of Zn(II) metal centers.⁴² For BPI_{Me}H, the pyridine arm is free to rotate out of the coordination pocket upon reduction; however, when a metal center is present, this rotation is likely inhibited. In the case of both metal complexes, the metal is present in the +1 oxidation state by the time the ligand reduction occurs. For Cu(I), the d¹⁰ electronic configuration would yield no crystal-field stabilization energy (CFSE) for coordination and we believe this results in rotation of the pyridine arm upon ligand reduction. For Ni(I), the d⁹ configuration could provide some level of CFSE and therefore the pyridine arm remains coordinated to the metal center on the timescale of the CV experiment, allowing for a reversible oxidation of the ligand.

Electrocatalysis

In the last few years tridentate pincer complexes of first-row transition metals have been used for electrocatalytic CO₂ reduction because of their high molecular tunability and, in some cases, ligand-based redox activity.^{5,28,54–57} To this end, the electrocatalytic activity of [Cu-BPI_{Me}]⁺ and [Ni-BPI_{Me}]⁺ toward CO₂ reduction were investigated in MeCN. Fig. 6 shows

Table 1 Summary of redox potentials for BPI_{Me}H, [Cu-BPI_{Me}]⁺, and [Ni-BPI_{Me}]⁺ in MeCN under N₂^a

	E _{pc1}	E _{pa1}	E _{1/2} (ΔE _p)	E _{pc2}	E _{pa2}	E _{1/2} (ΔE _p)	E _{pc3}	E _{pa3}	E _{1/2} (ΔE _p)
BPI _{Me} H				-1.76	-1.43	-1.59 (0.33)	-2.33	-2.17	-2.25 (0.16)
[Cu-BPI _{Me}] ⁺	-0.49	-0.28	-0.38 (0.21)	-1.82	-1.39	-1.60 (0.43)	-2.32	-2.20	-2.26 (0.12)
[Ni-BPI _{Me}] ⁺	-1.14	-1.05	-1.09 (0.09)	-1.84	-1.77	-1.82 (0.07)	-2.26	-2.02	-2.14 (0.24)

^a ΔE_p = E_{pa} - E_{pc}.

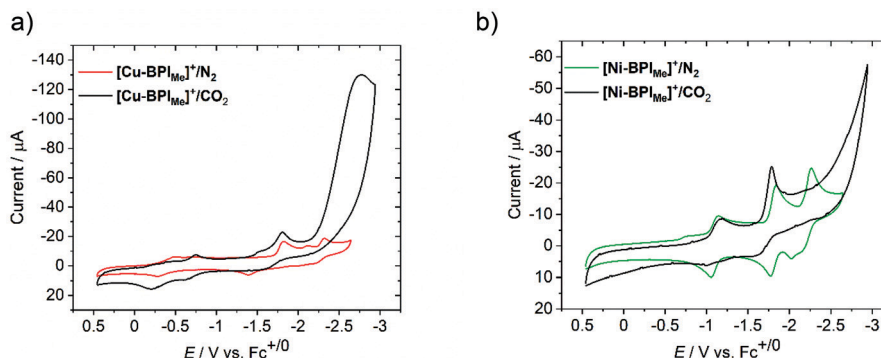


Fig. 6 CV data of (a) 0.5 mM [Cu-BPI_{Me}]⁺ and (b) 0.5 mM [Ni-BPI_{Me}]⁺ under N₂- and CO₂-saturated MeCN with 0.1 M TBAPF₆. Scan rate: 100 mV s⁻¹.

a comparison of these two complexes under N₂ and CO₂ atmospheres where some degree of electrocatalysis was observed in both cases. Scan rate dependent CVs for both complexes revealed that increases in current at potentials <−2.0 V are catalytic, exhibiting higher normalized current ($i/v^{1/2}$) at lower scan rates (Fig. S10†). For [Cu-BPI_{Me}]⁺, a large catalytic wave is found with $E_{pc} = -2.7$ V in addition to new features observed with $E_{1/2} = -0.7$ V and $E_{pc} = -1.8$ V. These latter features may indicate coordination of CO₂ to the copper complex. In the case of [Ni-BPI_{Me}]⁺, a small anodic shift and enhancement in current at the first ligand reduction was observed along with loss of the second ligand-based reduction feature and an exponential rise in current at potentials <−2.0 V. It is worth noting that the free ligand also displays some catalytic behavior for CO₂ reduction (Fig. S11†). Altogether, these data indicate that ligand reduction triggers catalysis.

Controlled potential electrolysis (CPE) experiments were performed for both complexes to determine reduced products and faradaic efficiencies (FE). Using a GC rod electrode and 0.5 mM [Cu-BPI_{Me}]⁺ or [Ni-BPI_{Me}]⁺ in CO₂-saturated MeCN, an applied potential of −2.45 V or −2.50 V, respectively, was held for upwards of 1 h. For both complexes, CO was found to be

the major product of CO₂ reduction with only small amounts of H₂ detected. Table 2 shows a summary of FE data as a function of electrolysis time for both complexes. Clearly, [Cu-BPI_{Me}]⁺ is more electrocatalytic, supported by the CV data of Fig. 6. The decrease in FE for H₂ in the case of [Cu-BPI_{Me}]⁺ is the result of continued electrolysis with no more appreciable increase in H₂. Likewise, the near constant FE for CO production at 11(±2)% in the case of [Ni-BPI_{Me}]⁺ points to a steady-state production of CO during the electrolysis period. In comparison, poor FE (<3%) for CO evolution was also observed by a nickel bis(aldimino)pyridine pincer complex.⁵⁶ Given the low FE for CO production for [Ni-BPI_{Me}]⁺, this complex was not explored further with electrocatalytic studies.

The FE for CO production in the case of [Cu-BPI_{Me}]⁺ makes a notable increase from 54(±2)% within the first ~15 min to 70(±1)% after this time point. Fig. 7a shows the charge accumulation during CPE where a sudden increase in charge was observed around the same time and coincided with the formation of a turbid solution. These observations suggested the formation of deposited material on the electrode surface which was also catalytic for CO₂ reduction to CO. After finishing the CPE experiment, the GC rod electrode appeared to have a brass colored, shiny deposition on the surface (Fig. S14†). The electrode was gently rinsed with acetone and scanned over the reductive potential window in fresh (absence of [Cu-BPI_{Me}]⁺) CO₂-saturated MeCN. The increase in current after the rinse test revealed deposition of a catalytically active material onto the electrode surface (Fig. S12†). Charge vs. time data obtained from CPE (−2.45 V) of the rinsed electrode are overlaid in Fig. 7a for comparison. The deposited material shows an immediate increase in charge with a similar slope to that observed after 15 min of electrolysis in the presence of [Cu-BPI_{Me}]⁺. Furthermore, the FE for CO with the rinsed electrode was consistently higher (75(±7)%) than [Cu-BPI_{Me}]⁺ in solution with no evidence for H₂ production (Table S10†). The deposited material eventually delaminated from the electrode surface, as evidenced by the leveling off of accumulated charge over time. CPE of [Ni-BPI_{Me}]⁺ also found evidence for a deposited material at the electrode surface (Fig. S14†) which was

Table 2 Summary of faradaic efficiencies (FE) for 0.5 mM complex in CO₂-saturated MeCN^a

Time (min)	[Cu-BPI _{Me}] ⁺ ^b		[Ni-BPI _{Me}] ⁺ ^c	
	FE for CO (%)	FE for H ₂ (%)	FE for CO (%)	FE for H ₂ (%)
5	52	6		
10	54	2	13	0
15	55	<1		
20			9	0
25	71	<1		
30			9	0
35	71	<1		
45	69	<1		
60			13	0

^a GC rod electrode, 0.1 M TBAPF₆. ^b −2.45 V. ^c −2.5 V.

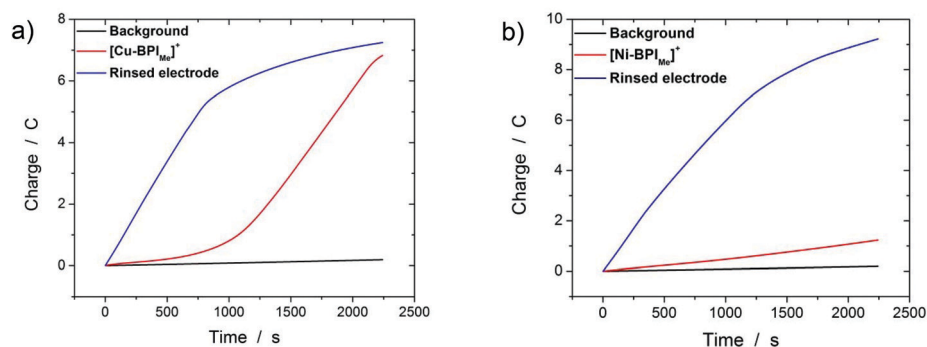


Fig. 7 Accumulated charge collected as a function of time during CPE of (a) 0.5 mM [Cu-BPI_{Me}]⁺ (−2.45 V) and (b) 0.5 mM [Ni-BPI_{Me}]⁺ (−2.50 V) in CO₂-saturated MeCN with 0.1 M TBAPF₆ using a GC rod electrode. Overlaid for each plot is the accumulated charge measured at the same applied potentials for the GC rod electrode after electrolysis. Electrodes were rinsed and CPE performed in a fresh CO₂-saturated MeCN solution in the absence of either complex.

catalytic for reduction of CO₂ to CO (Fig. 7b, Table S10†). FE's for CO production were found to be 83(±3)% over the first 25 min and began to decrease over time as the material delaminated from the electrode surface.

Electrocatalysis with [Cu-BPI_{Me}]⁺ was further explored in the presence of 5% H₂O added to the MeCN electrolyte. Water is a common source for protons needed in the reduction of CO₂ to CO as well as in the competitive formation of H₂. In the absence of added H₂O, protons are believed to be derived from trace water in the solvent and from the complex itself, which contains two coordinated water molecules in the solid state. CPE experiments were performed under these conditions and product yields monitored over time. At an applied potential of -2.3 V, the production of CO and H₂ were constant throughout the electrolysis period at 21(±4)% and 15(±2)% (Table S11†). These data indicate a competition between CO and H₂ formation with CO production decreasing with added H₂O. Furthermore, the presence of formate (HCO₂⁻) was detected by ¹H NMR at the end of the CPE experiment with an FE of 18% (Fig. S13†). The presence of formate suggests that a hydride intermediate may be present for the condition of added H₂O.⁵⁸⁻⁶¹ This would also support the competitive formation of H₂.

Electrodeposition of an unknown material was also observed for the condition of 5% H₂O and had a similar brass colored appearance as the deposited material in the absence of H₂O (Fig. S14†). CPE experiments using the rinsed electrode revealed a nearly constant FE for CO of 87(±4)% across the electrolysis period with no detectable formation of H₂ or formate (Table S11†). The FE for CO is slightly higher than that observed in the absence of water, however, we believe the deposited material to be the same in both cases.

Further experiments to understand the nature of surface deposition were conducted with GC disk electrodes so they could be analyzed by SEM and EDS following CPE experiments. SEM measurements on the GC disk electrode after 1 h of CPE (-2.67 V) in CO₂-saturated MeCN clearly showed a brass colored deposition on the electrode surface. SEM images of the electrode surface supported this observation (Fig. S15†) while EDS measurements revealed the deposited material contained a significant amount of copper (Table S12†). Notably, no evidence for deposition of nitrogen, which would be derived from the BPI_{Me}⁻ ligand, was observed. For comparison, EDS measurements for a GC disk subjected to CPE in the presence of [Ni-BPI_{Me}]⁺ showed the presence of nickel on the electrode surface in addition to carbon and oxygen. The detection of carbon is unavoidable based on the nature of the GC electrode, so we cannot say whether a carbonaceous species is deposited in either case, however, the measured oxygen content for both electrodes was greater than that observed for a clean GC electrode. This means we cannot rule out the presence of metal oxides (e.g. Cu₂O or NiO), but the color of the depositions strongly suggested metallic species.

The stability of [Cu-BPI_{Me}]⁺ and [Ni-BPI_{Me}]⁺ may be related to the reversibility of the ligand reduction. CV data shown in Fig. 5 and Table 1 indicate that the first ligand-based reduction was irreversible in the case of [Cu-BPI_{Me}]⁺, similar to

what was observed for free BPI_{Me}H, while the reduction was more reversible for [Ni-BPI_{Me}]⁺. Both complexes were observed to decompose during CPE experiments, however, the decomposition process appeared to be faster for [Cu-BPI_{Me}]⁺, as evidenced by the sudden increase in charge and FE for CO after 15 min. For [Ni-BPI_{Me}]⁺, a much lower amount of accumulated charge and FE for CO was observed during CPE. This could indicate slow decomposition of the complex.

Deposition of a heterogeneous catalysts is always a concern when studying molecular electrocatalysts. In the case of [Cu-BPI_{Me}]⁺, there are two relatively clear regimes for catalysis based on CPE data and measured FE's. In the first 15 min, we believe catalysis is largely homogeneous and [Cu-BPI_{Me}]⁺ is responsible for production of CO at 54(±2)% FE with the other 46% of current possibly contributing to decomposition. Experiments with 5% H₂O also clearly indicated homogeneous catalytic activity for the production of hydrogen and formate, showing neither of these products to be present after CPE experiments with the rinsed electrode. After 15 min, catalysis shifts from homogeneous to heterogeneous as indicated by the increase in charge and jump in FE for CO to 70(±1)%. This increase in FE would be consistent with deposition of copper metal, a well-known CO₂ reduction catalyst.⁶²⁻⁶⁸ Although CO is commonly observed as a product of copper metal catalysis, it is most notable for its ability to yield hydrocarbons and C-C bonded products in addition to operation in aqueous conditions.

Many examples of homogeneous molecular catalysts for CO₂ reduction to CO have been reported in the literature. The most extensively studied examples include Fe porphyrins, Ni cyclams, and [M(bpy)(CO)₃X]^{0/+} complexes where M = Re^I or Mn^I, bpy is 2,2'-bipyridine, and X is an anion or solvent.⁶⁹⁻⁷³ Onset potentials for CO₂ reduction with these catalysts range from -1.2 V vs. Fc⁺⁰ (Ni^{II}(cyclam)Cl₂) to -2.2 V vs. Fc⁺⁰ (Fe^{III}(tetraphenylporphyrin)Cl).^{70,74} [M(bpy)(CO)₃X]^{0/+} complexes fall in the middle of this range around -1.5 to -1.7 V depending on the functionalization of the bpy ligand.^{61,75-79} The present examples of [Cu-BPI_{Me}]⁺ and [Ni-BPI_{Me}]⁺ display onset potentials of -2.1 and -2.5 V respectively. These values are on the high end of the range reported above and we believe they could be tuned in the positive direction through functionalization of the BPI_{Me}⁻ ligand with electron withdrawing groups. Given the mixed homogeneous/heterogeneous catalytic behavior observed here, it is difficult to determine metrics for homogeneous catalysis such as turnover frequency and turnover number to make further comparisons with other catalysts in the literature.

Finally, the CO₂ reduction activity observed with [Cu-BPI_{Me}]⁺ is notable as molecular copper complexes are not commonly observed to display such reactivity. In addition, the few reported examples do not produce CO but instead produce oxalate (C₂O₄²⁻), a C-C bonded product.⁸⁰⁻⁸² In these examples, the coordination environment around the copper is distorted tetrahedral whereas the present example is trigonal bipyramidal. These results may suggest a structural selectivity for CO₂ reduction in copper coordination complexes.

Conclusions

In summary, this paper describes the synthesis and characterization of two pincer complexes of Cu(II) and Ni(II) with the bis(pyridylimino) isoindoline derived BPI_{Me}H ligand. Solid state X-ray crystallographic studies suggest that the position of steric methyl groups *ortho* to the pyridine nitrogen are important to preventing further coordination in the equatorial plane. Electrochemical studies of the free ligand, [Cu-BPI_{Me}]⁺, and [Ni-BPI_{Me}]⁺ under N₂ and CO₂ atmospheres reveal catalytic behavior for the reduction of CO₂ in all cases, where ligand-based reduction appears to be the initiation step for catalysis. Both complexes were found to produce CO as the reduced product with [Cu-BPI_{Me}]⁺ displaying higher catalytic activity than [Ni-BPI_{Me}]⁺. Both complexes are also shown to decompose into heterogeneous catalysts at the electrode surface. Based on physical appearance and EDS measurements, we believe these catalysts to be metallic copper and nickel, respectively, but cannot rule out the presence of metal oxides. The degradation of the complexes is believed to be the result of fluxional behavior in the ligand coordination of BPI_{Me}⁻, pointing to the importance of ligand rigidity in the design of first-row transition metal catalysts in low coordination environments.

Conflicts of interest

There are no conflicts to declare.

Acknowledgements

SS, AMS, MRM, and BHF acknowledge support from Auburn University as well as the National Science Foundation through a CAREER Award CHE-1945160. STS and JWJ thank the National Science Foundation for support through a CAREER Award CHE-1848478. The authors thank Dr John D. Gorden, Dr Melissa Boersma, and Alexandria Bredar for assistance with X-ray crystallography, ESI-MS, and SEM/EDS measurements, respectively.

References

- 1 F. Bertini, M. Glatz, B. Stöger, M. Peruzzini, L. F. Veiros, K. Kirchner and L. Gonsalvi, *ACS Catal.*, 2019, **9**, 632–639.
- 2 S. Chakraborty, P. Bhattacharya, H. Dai and H. Guan, *Acc. Chem. Res.*, 2015, **48**, 1995–2003.
- 3 M. Albrecht and G. van Koten, *Angew. Chem., Int. Ed.*, 2001, **40**, 3750–3781.
- 4 M. E. van der Boom and D. Milstein, *Chem. Rev.*, 2003, **103**, 1759–1792.
- 5 K. Talukdar, A. Issa and J. W. Jurss, *Front. Chem.*, 2019, **7**, 330.
- 6 J. Choi, A. H. R. MacArthur, M. Brookhart and A. S. Goldman, *Chem. Rev.*, 2011, **111**, 1761–1779.
- 7 G. Mancano, M. J. Page, M. Bhadbhade and B. A. Messerle, *Inorg. Chem.*, 2014, **53**, 10159–10170.
- 8 S. Hosokawa, J. Ito and H. Nishiyama, *Organometallics*, 2012, **31**, 8283–8290.
- 9 A. A. Danopoulos, N. Tsoureas, J. A. Wright and M. E. Light, *Organometallics*, 2004, **23**, 166–168.
- 10 E. Jürgens and D. Kunz, *Eur. J. Inorg. Chem.*, 2017, **2017**, 233–236.
- 11 M. Hernández-Juárez, M. Vaquero, E. Álvarez, V. Salazar and A. Suárez, *Dalton Trans.*, 2012, **42**, 351–354.
- 12 K. Umehara, S. Kuwata and T. Ikariya, *Inorg. Chim. Acta*, 2014, **413**, 136–142.
- 13 B. K. Langlotz, H. Wadepohl and L. H. Gade, *Angew. Chem., Int. Ed.*, 2008, **47**, 4670–4674.
- 14 V. C. Gibson, C. Redshaw and G. A. Solan, *Chem. Rev.*, 2007, **107**, 1745–1776.
- 15 W. O. Siegl, *J. Org. Chem.*, 1977, **42**, 1872–1878.
- 16 D. Benito-Garagorri and K. Kirchner, *Acc. Chem. Res.*, 2008, **41**, 201–213.
- 17 D. Benito-Garagorri, E. Becker, J. Wiedermann, W. Lackner, M. Pollak, K. Mereiter, J. Kisala and K. Kirchner, *Organometallics*, 2006, **25**, 1900–1913.
- 18 A. A. Kassie, P. Duan, M. B. Gray, K. Schmidt-Rohr, P. M. Woodward and C. R. Wade, *Organometallics*, 2019, **38**, 3419–3428.
- 19 J. J. Gair, Y. Qiu, R. L. Khade, N. H. Chan, A. S. Filatov, Y. Zhang and J. C. Lewis, *Organometallics*, 2019, **38**, 1407–1412.
- 20 M. A. Robinson, S. I. Trotz and T. J. Hurley, *Inorg. Chem.*, 1967, **6**, 392–394.
- 21 R. R. Gagne, R. S. Gall, G. C. Lisensky, R. E. Marsh and L. M. Speltz, *Inorg. Chem.*, 1979, **18**, 771–781.
- 22 R. R. Gagne, W. A. Marritt, D. N. Marks and W. O. Siegl, *Inorg. Chem.*, 1981, **20**, 3260–3267.
- 23 C. S. Sevov, S. L. Fisher, L. T. Thompson and M. S. Sanford, *J. Am. Chem. Soc.*, 2016, **138**, 15378–15384.
- 24 M. L. Buil, M. A. Esteruelas, S. Izquierdo, A. I. Nicasio and E. Oñate, *Organometallics*, 2020, **39**, 2719–2731.
- 25 T. Váradi, J. S. Pap, M. Giorgi, L. Párkányi, T. Csay, G. Speier and J. Kaizer, *Inorg. Chem.*, 2013, **52**, 1559–1569.
- 26 J. Kaizer, G. Baráth, G. Speier, M. Réglie and M. Giorgi, *Inorg. Chem. Commun.*, 2007, **10**, 292–294.
- 27 M. Bröring and C. Kleeberg, *Chem. Commun.*, 2008, 2777–2778.
- 28 F.-W. Liu, J. Bi, Y. Sun, S. Luo and P. Kang, *ChemSusChem*, 2018, **11**, 1656–1663.
- 29 D. C. Sauer, H. Wadepohl and L. H. Gade, *Inorg. Chem.*, 2012, **51**, 12948–12958.
- 30 M. Szávuly, R. Csonka, G. Speier, R. Barabás, M. Giorgi and J. Kaizer, *J. Mol. Catal. A: Chem.*, 2014, **392**, 120–126.
- 31 A. L. Müller, T. Bleith, T. Roth, H. Wadepohl and L. H. Gade, *Organometallics*, 2015, **34**, 2326–2342.
- 32 K.-N. T. Tseng, J. W. Kampf and N. K. Szymczak, *Organometallics*, 2013, **32**, 2046–2049.
- 33 W. R. Hagen, *Biomolecular EPR Spectroscopy*, CRC Press, 2008.

- 34 G. M. Sheldrick, *Acta Crystallogr., Sect. A: Found. Crystallogr.*, 2008, **64**, 112–122.
- 35 *DOC-M86-EXX229 V1 APEX3 Crystallography Software Suite User Manual*. Bruker AXS Inc., Madison, Wisconsin, 2016.
- 36 K. Gogoi, S. Saha, B. Mondal, H. Deka, S. Ghosh and B. Mondal, *Inorg. Chem.*, 2017, **56**, 14438–14445.
- 37 R. Csonka, G. Speier and J. Kaizer, *RSC Adv.*, 2015, **5**, 18401–18419.
- 38 L. Gianelli, V. Amendola, L. Fabbrizzi, P. Pallavicini and G. G. Mellerio, *Rapid Commun. Mass Spectrom.*, 2001, **15**, 2347–2353.
- 39 H. Lavanant, H. Virelizier and Y. Hoppilliard, *J. Am. Soc. Mass Spectrom.*, 1998, **9**, 1217–1221.
- 40 Y.-Z. Hao, Y. Xu, X.-H. Wei and H.-B. Tong, *Acta Crystallogr., Sect. E: Struct. Rep. Online*, 2007, **63**, o1549–o1550.
- 41 T. Csay, B. Kripli, M. Giorgi, J. Kaizer and G. Speier, *Inorg. Chem. Commun.*, 2010, **13**, 227–230.
- 42 O. P. Anderson, A. la Cour, A. Dodd, A. D. Garrett and M. Wicholas, *Inorg. Chem.*, 2003, **42**, 122–127.
- 43 A. M. Herrera, R. J. Staples, S. V. Kryatov, A. Y. Nazarenko and E. V. Rybak-Akimova, *Dalton Trans.*, 2003, 846–856.
- 44 M. B. Meder and L. H. Gade, *Eur. J. Inorg. Chem.*, 2004, **2004**, 2716–2722.
- 45 J. Kaizer, J. Pap, G. Speier and L. Párkányi, *Z. Kristallogr. - New Cryst. Struct.*, 2004, **219**, 141–142.
- 46 B. L. Truesdell, T. B. Hamby and C. S. Sevov, *J. Am. Chem. Soc.*, 2020, **142**, 5884–5893.
- 47 J. D. Dang and T. P. Bender, *Inorg. Chem. Commun.*, 2013, **30**, 147–151.
- 48 R. N. Jones, *Chem. Rev.*, 1947, **41**, 353–371.
- 49 K. Hanson, L. Roskop, P. I. Djurovich, F. Zahariev, M. S. Gordon and M. E. Thompson, *J. Am. Chem. Soc.*, 2010, **132**, 16247–16255.
- 50 H.-M. Wen, Y.-H. Wu, Y. Fan, L.-Y. Zhang, C.-N. Chen and Z.-N. Chen, *Inorg. Chem.*, 2010, **49**, 2210–2221.
- 51 M. Corbett and B. F. Hoskins, *J. Am. Chem. Soc.*, 1967, **89**, 1530–1532.
- 52 E. Garribba and G. Micera, *J. Chem. Educ.*, 2006, **83**, 1229.
- 53 B. J. Hathaway and A. A. G. Tomlinson, *Coord. Chem. Rev.*, 1970, **5**, 1–43.
- 54 M. Sheng, N. Jiang, S. Gustafson, B. You, D. H. Ess and Y. Sun, *Dalton Trans.*, 2015, **44**, 16247–16250.
- 55 T. H. T. Myren, A. M. Lilio, C. G. Huntzinger, J. W. Horstman, T. A. Stinson, T. B. Donadt, C. Moore, B. Lama, H. H. Funke and O. R. Luca, *Organometallics*, 2019, **38**, 1248–1253.
- 56 R. Narayanan, M. McKinnon, B. R. Reed, K. T. Ngo, S. Groysman and J. Rochford, *Dalton Trans.*, 2016, **45**, 15285–15289.
- 57 J. D. Cope, N. P. Liyanage, P. J. Kelley, J. A. Denny, E. J. Valente, C. E. Webster, J. H. Delcamp and T. K. Hollis, *Chem. Commun.*, 2017, **53**, 9442–9445.
- 58 A. Taheri and L. A. Berben, *Chem. Commun.*, 2016, **52**, 1768–1777.
- 59 B. M. Ceballos, C. Tsay and J. Y. Yang, *Chem. Commun.*, 2017, **53**, 7405–7408.
- 60 K. M. Waldie, A. L. Ostericher, M. H. Reineke, A. F. Sasayama and C. P. Kubiak, *ACS Catal.*, 2018, **8**, 1313–1324.
- 61 S. S. Roy, K. Talukdar and J. W. Jurss, *ChemSusChem*, 2020, **13**, 1–10.
- 62 F. S. Roberts, K. P. Kuhl and A. Nilsson, *Angew. Chem., Int. Ed.*, 2015, **127**, 5268–5271.
- 63 S. Nitopi, E. Bertheussen, S. B. Scott, X. Liu, A. K. Engstfeld, S. Horch, B. Seger, I. E. L. Stephens, K. Chan, C. Hahn, J. K. Nørskov, T. F. Jaramillo and I. Chorkendorff, *Chem. Rev.*, 2019, **119**, 7610–7672.
- 64 A. J. Garza, A. T. Bell and M. Head-Gordon, *ACS Catal.*, 2018, **8**, 1490–1499.
- 65 D. Kopač, B. Likozar and M. Huš, *Appl. Surf. Sci.*, 2019, **497**, 143783.
- 66 J. Zhao, S. Xue, J. Barber, Y. Zhou, J. Meng and X. Ke, *J. Mater. Chem. A*, 2020, **8**, 4700–4734.
- 67 C. S. Chen, A. D. Handoko, J. H. Wan, L. Ma, D. Ren and B. S. Yeo, *Catal. Sci. Technol.*, 2014, **5**, 161–168.
- 68 C. W. Li and M. W. Kanan, *J. Am. Chem. Soc.*, 2012, **134**, 7231–7234.
- 69 C. Costentin, S. Drouet, M. Robert and J.-M. Savéant, *Science*, 2012, **338**, 90–94.
- 70 M. Beley, J.-P. Collin, R. Ruppert and J.-P. Sauvage, *J. Chem. Soc., Chem. Commun.*, 1984, 1315–1316.
- 71 J. Hawecker, J.-M. Lehn and R. Ziessel, *J. Chem. Soc., Chem. Commun.*, 1983, 536–538.
- 72 C. Riplinger, M. D. Sampson, A. M. Ritzmann, C. P. Kubiak and E. A. Carter, *J. Am. Chem. Soc.*, 2014, **136**, 16285–16298.
- 73 E. E. Benson, C. P. Kubiak, A. J. Sathrum and J. M. Smieja, *Chem. Soc. Rev.*, 2008, **38**, 89–99.
- 74 M. Hammouche, D. Lexa, M. Momenteau and J. M. Saveant, *J. Am. Chem. Soc.*, 1991, **113**, 8455–8466.
- 75 K. Talukdar, S. Sinha Roy, E. Amatya, E. A. Sleeper, P. Le Magueres and J. W. Jurss, *Inorg. Chem.*, 2020, **59**, 6087–6099.
- 76 A. Zhanaidarova, A. L. Ostericher, C. J. Miller, S. C. Jones and C. P. Kubiak, *Organometallics*, 2019, **38**, 1204–1207.
- 77 J. Hawecker, J.-M. Lehn and R. Ziessel, *J. Chem. Soc., Chem. Commun.*, 1984, 328–330.
- 78 M. H. Rønne, D. Cho, M. R. Madsen, J. B. Jakobsen, S. Eom, É. Escoudé, H. C. D. Hammershøj, D. U. Nielsen, S. U. Pedersen, M.-H. Baik, T. Skrydstrup and K. Daasbjerg, *J. Am. Chem. Soc.*, 2020, **142**, 4265–4275.
- 79 K. T. Ngo, M. McKinnon, B. Mahanti, R. Narayanan, D. C. Grills, M. Z. Ertem and J. Rochford, *J. Am. Chem. Soc.*, 2017, **139**, 2604–2618.
- 80 U. R. Pokharel, F. R. Fronczek and A. W. Maverick, *Nat. Commun.*, 2014, **5**, 5883.
- 81 B. J. Cook, G. N. Di Francesco, K. A. Abboud and L. J. Murray, *J. Am. Chem. Soc.*, 2018, **140**, 5696–5700.
- 82 R. Angamuthu, P. Byers, M. Lutz, A. L. Spek and E. Bouwman, *Science*, 2010, **327**, 313–315.